Unconditionally stable method and numerical solution of the hyperbolic phase-field crystal equation

P. K. Galenko*
Friedrich-Schiller-Universität Jena, Physikalisch-Astronomische Fakultät, D-07737 Jena, Germany

H. Gomez
Department of Mathematical Methods, University of A Coruña, Campus de Elviña, s/n, 15192 A Coruña, Spain

N. V. Kropotin
Institut für Materialphysik im Weltraum, Deutsches Zentrum für Luft- und Raumfahrt (DLR), 51170 Köln, Germany

K. R. Elder
Department of Physics, Oakland University, Rochester, Michigan 48309-4487, USA
(Received 14 April 2013; published 26 July 2013)

The phase-field crystal model (PFC model) resolves systems on atomic length scales and diffusive time scales and lies in between standard phase-field modeling and atomistic methods. More recently a hyperbolic or modified PFC model was introduced to describe fast (propagative) and slow (diffusive) dynamics. We present a finite-element method for solving the hyperbolic PFC equation, introducing an unconditionally stable time integration algorithm. A spatial discretization is used with the traditional C^0-continuous Lagrange elements with quadratic shape functions. The space-time discretization of the PFC equation is second-order accurate in time and is shown analytically to be unconditionally stable. Numerical simulations are used to show a monotonic decrease of the free energy during the transition from the homogeneous state to stripes. Benchmarks on modeling patterns in two-dimensional space are carried out. The benchmarks show the applicability of the proposed algorithm for determining equilibrium states. Quantitatively, the proposed algorithm is verified for the problem of lattice parameter and velocity selection when a crystal invades a homogeneous unstable liquid.

DOI: 10.1103/PhysRevE.88.013310 PACS number(s): 02.70.−c, 05.70.Fh, 05.70.Ln, 64.60.−i

I. INTRODUCTION

The phase-field crystal model (PFC model) is a continuum model that describes processes on atomic length scales and patterns on the nanolength and microlength scales [1–3]. This model is characterized by a conserved field that is related to the local atomic number density, such that it is spatially periodic in the solid phase and constant in the liquid phase. The model has been related to other continuum field theories such as classical density-functional theory [4,5] and the atomic density function theory [6]. The PFC model provides an efficient tool for simulating the ordering of nanoscale structures on micron length scales [3], liquid-solid transitions, dislocation motion and plasticity, glass formation and foams, epitaxial growth, grain boundary premelting, crack propagation, surface reconstructions, grain boundary energies, dynamics of colloidal systems, and polymers (for an overview, see Ref. [7] and the references therein).

Originally formulated in a parabolic form, the PFC model has now been extended to include faster degrees of freedom consistent with inertia due to propagative regimes of transformation. In particular, a hyperbolic or modified PFC model was introduced which includes an inertial term, and thus allows for the description of both fast and slow dynamics of transformation [8–10]. Fast front dynamics occurs when a system is quenched far below a transition point or far below the equilibrium temperature of the phase transition. These conditions lead to a fast phase transition when the velocity of the front is comparable to the speed of atomic diffusion or the speed of local structural relaxation. The movement of a phase transition front at such fast velocities can lead to the formation of bulk phases that are not in a local structural or chemical equilibrium.

The fascinating physics captured by the hyperbolic PFC model has triggered a growing interest in the development of computational methods to solve the equation. From a numerical analysis perspective, algorithms for solving the hyperbolic PFC model have to contend with first- and second-order time derivatives and six-order spatial derivatives. Therefore, several special numerical methods for the solution of the hyperbolic PFC equation were recently developed. Wise *et al.* [11] derived a first-order accurate and unconditionally energy stable finite-difference scheme based on a convex splitting of a discrete energy for the parabolic PFC equation. Similar concepts were applied to the hyperbolic Cahn-Hilliard and Allen-Cahn equations in Ref. [12]. Subsequently, a second-order accurate finite-difference method was introduced [13,14], which is unconditionally stable with respect to a discrete version of a quantity entitled as "pseudoenergy."

In the present paper, we concentrate on the development of a finite-element method for the hyperbolic PFC equation, introducing a new unconditionally stable time integration algorithm. A space-time discretization of the hyperbolic PFC equation which is second-order time accurate and unconditionally stable is proposed. Unconditional stability in this context means that the free energy of the discrete solution decreases (or remains constant) from one step to the next irrespective

*Peter.Galenko@uni-jena.de

of the mesh size and the time step. This implies that the algorithm respects the underlying physics of the equation. From a practical point of view, unconditional stability is associated with increased robustness, better behavior of the numerical solution for large time steps, and higher accuracy for long-time calculations. The most common paradigm for achieving unconditional stability in the context of phase transition problems is the so-called Eyre's method [15,16], which is widely used in computational physics [17,18]. Although Eyre's method was a significant step forward, it has been recently shown that it leads to inaccurate solutions for large time steps [19] because it is only a first-order accurate method. Recently, a generalization of Eyre's method that achieves unconditional stability has been introduced, but in contrast with Eyre's method, it is second-order accurate [19,20]. This generalization has been applied to the PFC equation [20], using a space discretization that requires the use of globally C^1-continuous finite elements [21]. In the present work this algorithm is extended to the hyperbolic (modified) PFC equation. We introduce a space discretization that can be used with traditional C^0-continuous Lagrange finite elements, available in all finite-element software packages. As an example, the proposed algorithm is applied to the problem of the lattice parameter and velocity selection when a periodic crystal front invades homogeneous liquid phase.

The paper is organized as follows. The hyperbolic or modified PFC-equation is formulated in Section II. To have a finite-element discretization of the modified PFC equation, a splitting and a variational formulation of the equation are presented in Sec. III. Spatial and temporal discretization of the equations are shown in Sec. IV. A numerical approximation of the discrete form is given in Sec. V using triangular Lagrange elements. In Sec. VI we present tests for the numerical scheme. Results on the phase diagram and free energy of the entire system are summarized. Section VII is devoted to the numerical solution of the problem of the wave number and velocity selection of a front invading an unstable phase. Numerical results for the front velocity and wave number at the front are compared to those obtained previously using marginal stability analysis. Finally, Sec. VIII presents a summary of our conclusions.

II. MODIFIED PFC EQUATION

Let ϕ be a continuous field describing an atomic-scale density. We consider the following free energy functional [12,22]

$$\mathcal{F}[\phi,\vec{J}] = \mathcal{F}_{\rm eq}[\phi] + \mathcal{F}_{\rm neq}[\vec{J}], \tag{1}$$

with the local equilibrium contribution

$$\mathcal{F}_{\rm eq}[\phi] = \int_\Omega \left[F(\phi) - |\vec{\nabla}\phi|^2 + \frac{1}{2}(\nabla^2\phi)^2 \right] d\Omega, \tag{2}$$

and the following pure nonequilibrium contribution

$$\mathcal{F}_{\rm neq}[\vec{J}] = \frac{\tau}{2}\int_\Omega \vec{J}\cdot\vec{J}\,d\Omega, \quad \tau > 0. \tag{3}$$

In Eq. (2) the homogeneous (space independent) part of the free energy density is given by

$$F(\phi) = \frac{1-\varepsilon}{2}\phi^2 + \frac{\alpha}{3}\phi^3 + \frac{1}{4}\phi^4, \tag{4}$$

while, in Eq. (3), $\vec{J}$ is a vector field of the flux that satisfies the conservation equation

$$\frac{\partial\phi}{\partial t} + \vec{\nabla}\cdot\vec{J} = 0, \tag{5}$$

where t denotes the time. For the free energy functional defined in Eq. (1) to decrease or remain constant in time the vector field $\vec{J}$ needs to fulfill the relation

$$\tau\frac{\partial\vec{J}}{\partial t} + \vec{J} = -\vec{\nabla}\mu, \tag{6}$$

where the chemical potential μ is given by

$$\mu(\phi) \equiv \frac{\delta\mathcal{F}}{\delta\phi} = \frac{dF(\phi)}{d\phi} + 2\nabla^2\phi + \nabla^4\phi, \tag{7}$$

with

$$\frac{dF(\phi)}{d\phi} = \phi^3 + \alpha\phi^2 + (1-\varepsilon)\phi \equiv f(\phi). \tag{8}$$

In the above expressions, $\varepsilon = (T_c - T)/T_c$ is the governing parameter which characterizes undercooling, T and T_c are the temperature and the critical temperature of the transition, respectively, and τ is the relaxation time of the flux $\vec{J}$ to its stationary state. The free energy density (4) can describe transitions from metastable (as occurs close to first-order phase transitions, e.g., in solidification processes) and unstable states (as occurs in second-order phase transitions) to stable ones.

The system of Eqs. (5) and (6) can be rewritten in the form

$$\tau\frac{\partial^2\phi}{\partial t^2} + \frac{\partial\phi}{\partial t} = \nabla^2\mu. \tag{9}$$

The hyperbolic equation (9) includes the dissipation described by the traditional parabolic PFC equation [1], as well as an inertial term $\propto\partial^2\phi/\partial t^2$ that accounts for the kinetic contribution (3). Alternatively, Eq. (9) was proposed by Stefanovic *et al.* [8] to incorporate both fast elastic relaxation and slower mass diffusion.

Introducing the new variable ψ, one can split Eq. (9) as

$$\begin{cases} \dfrac{\partial\phi}{\partial t} = \psi, \\ \tau\dfrac{\partial\psi}{\partial t} = \nabla^2\mu - \psi. \end{cases} \tag{10}$$

Using the Helmholtz decomposition theorem, the flux $\vec{J}$ can be unambiguously defined through the expansion of gradient and curl contributions: $\vec{J} = -\vec{\nabla}u + \vec{\nabla}\times\vec{U}$. Now, we notice that the dynamics of the phase variable ϕ is only determined by the divergence of $\vec{J}$ [12], so one can take the divergence of Eq. (6), and use the Helmoholtz decomposition of $\vec{J}$ in Eq. (5) to derive the system of partial differential equations

$$\begin{cases} \dfrac{\partial\phi}{\partial t} = \nabla^2 u, \\ \tau\dfrac{\partial\nabla^2 u}{\partial t} = \nabla^2\mu - \nabla^2 u, \\ \mu = f(\phi) + 2\nabla^2\phi + \nabla^4\phi. \end{cases} \tag{11}$$

The system of equations (11) is equivalent to the hyperbolic equation (9), and represents a convenient form for developing an unconditionally stable computational schemes [12,13].

While in principle an equation for the curl of $\vec{J}$ could also be included it is not of much interest since it does not couple to ϕ and decays exponentially in time in such a manner that $\mathcal{F}_{\text{neq}}$ always decreases. Thus the contribution of $\vec{\nabla}\times\vec{U}$ to $\vec{J}$ can be ignored.

III. VARIATIONAL FORMULATION

In this section we introduce a variational formulation of the modified phase field crystal equation with the ultimate goal of deriving a finite-element discretization. To implement a classical Lagrange finite-element scheme it is convenient to introduce the variable θ, such that $\theta=\nabla^2\phi$, and, following Eqs. (11), we solve the system of equations

$$\begin{cases} \dfrac{\partial\phi}{\partial t}=\nabla^2 u, \\ \tau\dfrac{\partial\nabla^2 u}{\partial t}=\nabla^2\mu-\nabla^2 u, \\ \mu=f(\phi)+2\nabla^2\phi+\nabla^2\theta, \\ \dfrac{\partial\theta}{\partial t}=\dfrac{\partial\nabla^2\phi}{\partial t}. \end{cases} \tag{12}$$

The variational problem associated with the system of equations (12) is stated as follows: find ϕ, u, μ, θ such that for all v, w, p, q the following system of equations is satisfied

$$\begin{cases} \displaystyle\int_\Omega v\frac{\partial\phi}{\partial t}d\Omega+\int_\Omega\vec{\nabla}v\cdot\vec{\nabla}u d\Omega=0, \\ \displaystyle-\int_\Omega\tau\vec{\nabla}w\cdot\frac{\partial\vec{\nabla}u}{\partial t}d\Omega+\int_\Omega\vec{\nabla}w\cdot\vec{\nabla}\mu d\Omega-\int_\Omega\vec{\nabla}w\cdot\vec{\nabla}u d\Omega=0, \\ \displaystyle\int_\Omega p[\mu-f(\phi)]d\Omega+\int_\Omega 2\vec{\nabla}p\cdot\vec{\nabla}\phi d\Omega+\int_\Omega\vec{\nabla}p\cdot\vec{\nabla}\theta d\Omega=0, \\ \displaystyle\int_\Omega q\frac{\partial\theta}{\partial t}d\Omega+\int_\Omega\vec{\nabla}q\cdot\frac{\partial\vec{\nabla}\phi}{\partial t}d\Omega=0, \end{cases} \tag{13}$$

which assumes free-flux conditions for all variables on the surface Γ for the volume Ω. Due to their integral form, Eqs. (13) present a weak form of differential equations (12).

We show now that Eqs. (13), which are equivalent to the modified PFC equation (9), lead to a stable evolution of the system such that the free energy of the entire system does not increase in time, i.e.,

$$\frac{d\mathcal{F}(\phi,\vec{J})}{dt}=\int_\Omega\left(\frac{\delta\mathcal{F}}{\delta\phi}\frac{\partial\phi}{\partial t}+\frac{\delta\mathcal{F}}{\delta\vec{J}}\cdot\frac{\partial\vec{J}}{\partial t}\right)d\Omega\leqslant 0. \tag{14}$$

Using the balance (5), one can obtain from Eqs. (1) and (3) that the free energy (14) is given by

$$\begin{aligned}\frac{d\mathcal{F}(\phi,\vec{J})}{dt}&=-\int_\Omega\mu\vec{\nabla}\cdot\vec{J}d\Omega+\int_\Omega\tau\vec{J}\cdot\frac{\partial\vec{J}}{\partial t}d\Omega \\ &=\int_\Omega\mu\frac{\partial\phi}{\partial t}d\Omega+\int_\Omega\tau\vec{J}\cdot\frac{\partial\vec{J}}{\partial t}d\Omega,\end{aligned} \tag{15}$$

with $\vec{J}=0$ on Γ. Taking $v=\mu$, and $w=u$ in Eq. (13) and combining the first two equations, one gets

$$\int_\Omega\mu\frac{\partial\phi}{\partial t}d\Omega+\int_\Omega\tau\vec{\nabla}u\cdot\frac{\partial\vec{\nabla}u}{\partial t}d\Omega+\int_\Omega\vec{\nabla}u\cdot\vec{\nabla}u d\Omega=0. \tag{16}$$

The first equation in Eqs. (11) and the balance (5) lead to $\vec{\nabla}\cdot(\vec{J}+\vec{\nabla}u)=0$. Using again the Helmholtz decomposition of $\vec{J}$, we note that the last equation is unaffected by the term $\vec{\nabla}\times\vec{U}$, so we may just take

$$\vec{J}=-\vec{\nabla}u. \tag{17}$$

Substituting the later relation between $\vec{J}$ and u into Eq. (15) gives

$$\frac{d\mathcal{F}(\phi,\vec{J})}{dt}=\int_\Omega\mu\frac{\partial\phi}{\partial t}d\Omega+\int_\Omega\tau\vec{\nabla}u\cdot\vec{\nabla}\frac{\partial u}{\partial t}d\Omega. \tag{18}$$

Comparing Eq. (18) with Eq. (16) we obtain the stability condition

$$\frac{d\mathcal{F}(\phi,\vec{J})}{dt}=-\int_\Omega\vec{\nabla}u\cdot\vec{\nabla}u d\Omega\leqslant 0, \tag{19}$$

which confirms Eq. (14) for the stable evolution of the entire system.

In consideration of the variational formulation (13) we have now shown an important feature of the free energy $\mathcal{F}$ which has classical contribution consistent with the local equilibrium processes and the additional kinetic contribution for the description of fast transitions on the scale of τ, Eq. (1). Namely, the sign of the free energy time derivative in Eqs. (14) and (19) shows that $\mathcal{F}$ can be considered as a Lyapunov function: a function that is nonincreasing in time and determines the stability of the system.

IV. STABLE NUMERICAL SCHEME

A. Discretization

We now discretize the variational form (13) replacing the relevant functions with their discrete counterparts that will be

denoted with an h superscript. Then it follows that

$$\begin{cases} \int_\Omega v^h \dfrac{\partial \phi^h}{\partial t} d\Omega + \int_\Omega \vec{\nabla} v^h \cdot \vec{\nabla} u^h d\Omega = 0, \\ -\int_\Omega \tau \vec{\nabla} w^h \cdot \dfrac{\partial \vec{\nabla} u^h}{\partial t} d\Omega + \int_\Omega \vec{\nabla} w^h \cdot \vec{\nabla} \mu^h d\Omega - \int_\Omega \vec{\nabla} w^h \cdot \vec{\nabla} u^h d\Omega = 0, \\ \int_\Omega p^h [\mu^h - f(\phi^h)] d\Omega + \int_\Omega 2\vec{\nabla} p^h \cdot \vec{\nabla} \phi^h d\Omega + \int_\Omega \vec{\nabla} p^h \cdot \vec{\nabla} \theta^h d\Omega = 0, \\ \int_\Omega q^h \dfrac{\partial \theta^h}{\partial t} d\Omega + \int_\Omega \vec{\nabla} q^h \cdot \dfrac{\partial \vec{\nabla} \phi^h}{\partial t} d\Omega = 0. \end{cases} \tag{20}$$

The system of equations (20) is a semidiscretized numerical scheme, i.e., it represents the spatial discretization of Eqs. (13).

To obtain the time discretization algorithm, the time interval of interest $[0,T]$ is subdivided into N uniform subintervals $\mathcal{I}_n = (t_n, t_{n+1})$ where $t_{n+1} - t_n = \Delta t$; $n = 0, \ldots, N-1$. The discrete approximation of $\phi^h(t_n)$ is notated as ϕ^h_n, where the dependence on the spatial coordinate is omitted for simplicity. Analogous notation is used for other functions of interest. Special notations $\{\{\phi^h_n\}\} = \phi^h_{n+1} - \phi^h_n$ and $\phi^h_{n+1/2} = \frac{1}{2}(\phi^h_{n+1} + \phi^h_n)$ are also used below. We propose an algorithm which may be thought of as a second-order accurate generalization of Eyre's method [15]. However, rather than splitting the free energy into a concave and convex parts as in Eyre's method, we split it as follows:

$$F(\phi) = F_+(\phi) + F_-(\phi), \tag{21}$$

where $F^{(iv)}_+(\phi) \geqslant 0$, $F^{(iv)}_-(\phi) \leqslant 0$, and the superscript (iv) denotes the fourth derivative. The advantage of this splitting over Eyre's splitting is that it permits deriving a second-order accurate and unconditionally stable method in contrast to Eyre's method which is only first-order accurate. As shown for the dynamics of phase separation [19], the use of a second-order accurate method permits taking time steps several orders of magnitude larger than those required by the first-order accurate method. We also note that, although for the modified phase field crystal equation, in which one gets $F_- = 0$, we will present the method in its full generality, assuming that both F_+ and F_- are nonzero. The general method would be useful, for example, for PFC equations, based on logarithmic potentials (which give $F_- \neq 0$). We will also use the notation $f_+(\phi) = F'_+(\phi)$ and $f_-(\phi) = F'_-(\phi)$. Then, our algorithm, Eqs. (20), may be written as follows:

$$\begin{cases} \int_\Omega v^h \dfrac{\{\{\phi^h_n\}\}}{\Delta t} d\Omega + \int_\Omega \vec{\nabla} v^h \cdot \vec{\nabla} u^h_{n+1/2} d\Omega = 0, \\ -\int_\Omega \tau \vec{\nabla} w^h \cdot \dfrac{\{\{\vec{\nabla} u^h_n\}\}}{\Delta t} d\Omega + \int_\Omega \vec{\nabla} w^h \cdot \vec{\nabla} \mu^h_{n+1/2} d\Omega - \int_\Omega \vec{\nabla} w^h \cdot \vec{\nabla} u^h_{n+1/2} d\Omega = 0, \\ \int_\Omega p^h \mu^h_{n+1/2} d\Omega - \int_\Omega p^h \dfrac{1}{2}\left[f(\phi^h_{n+1}) + f(\phi^h_n)\right] d\Omega + \int_\Omega p^h \dfrac{\{\{\phi^h_n\}\}^2}{12}\left[f''_+(\phi^h_n) + f''_-(\phi^h_{n+1})\right] d\Omega \\ + \int_\Omega 2\vec{\nabla} p^h \cdot \vec{\nabla} \phi^h_{n+1/2} d\Omega + \int_\Omega \vec{\nabla} p^h \cdot \vec{\nabla} \theta^h_{n+1/2} d\Omega = 0, \\ \int_\Omega q^h \dfrac{\{\{\theta^h_n\}\}}{\Delta t} d\Omega + \int_\Omega \vec{\nabla} q^h \cdot \vec{\nabla}\left(\dfrac{\{\{\phi^h_n\}\}}{\Delta t}\right) d\Omega = 0. \end{cases} \tag{22}$$

The system of equations (22) is a fully discretized numerical scheme, i.e., it represents the temporal and spatial discretization of Eqs. (13). As we will see in the next section, the appearance of the second and third terms in the third equation lead to an unconditionally stable discretization of the nonlinear term.

B. Stability

To show that the algorithm inherits the stability condition of the continuous theory, $d\mathcal{F}/dt < 0$ [see Eqs. (14) and (19)], we need to take into account the following quadrature formulas: Let $g : [a,b] \mapsto R$ be a sufficiently smooth function. The following relations hold [19]:

$$\int_a^b g(x)dx = \frac{b-a}{2}[g(a) + g(b)] - \frac{(b-a)^3}{12} g''(a) - \frac{(b-a)^4}{24} g'''(\chi_+); \quad \chi_+ \in (a,b), \tag{23}$$

$$\int_a^b g(x)dx = \frac{b-a}{2}[g(a) + g(b)] - \frac{(b-a)^3}{12} g''(b) + \frac{(b-a)^4}{24} g'''(\chi_-); \quad \chi_- \in (a,b). \tag{24}$$

Let us consider the trivial identity

$$\int_{\phi_n^h}^{\phi_{n+1}^h} F_+'(z)dz = \int_{\phi_n^h}^{\phi_{n+1}^h} f_+(z)dz. \tag{25}$$

If we integrate directly the left-hand side of the equation, and apply the quadrature formula (23) to the right-hand side, we obtain

$$\{\{F_+(\phi_n^h)\}\} = \frac{\{\{\phi_n^h\}\}}{2}\left[f_+(\phi_n^h) + f_+(\phi_{n+1}^h)\right] - \frac{\{\{\phi_n^h\}\}^3}{12} f_+''(\phi_n^h) - \frac{\{\{\phi_n^h\}\}^2}{24} f_+'''(\phi_{n+\xi_+}^h), \quad \xi_+ \in (0,1). \tag{26}$$

Rearranging Eq. (26), it follows that

$$\frac{\{\{F_+(\phi_n^h)\}\}}{\{\{\phi_n^h\}\}} + \frac{\{\{\phi_n^h\}\}^3}{24} f_+'''(\phi_{n+\xi_+}^h) = \frac{1}{2}\left[f_+(\phi_n^h) + f_+(\phi_{n+1}^h)\right] - \frac{\{\{\phi_n^h\}\}^2}{12} f_+''(\phi_n^h), \quad \xi_+ \in (0,1). \tag{27}$$

Analogously, applying quadrature (24) to the identity

$$\int_{\phi_n^h}^{\phi_{n+1}^h} F_-'(z)dz = \int_{\phi_n^h}^{\phi_{n+1}^h} f_-(z)dz, \tag{28}$$

and operating, one obtains

$$\frac{\{\{F_-(\phi_n^h)\}\}}{\{\{\phi_n^h\}\}} - \frac{\{\{\phi_n^h\}\}^3}{24} f_-'''(\phi_{n+\xi_-}^h) = \frac{1}{2}\left[f_-(\phi_n^h) + f_-(\phi_{n+1}^h)\right] - \frac{\{\{\phi_n^h\}\}^2}{12} f_-''(\phi_{n+1}^h); \quad \xi_- \in (0,1). \tag{29}$$

We now show that with the choices

$$v^h = \mu_{n+1/2}^h, \quad w^h = u_{n+1/2}^h, \quad p^h = \frac{\{\{\phi_n^h\}\}}{\Delta t}, \quad q^h = \theta_{n+1/2}^h, \tag{30}$$

the stability condition is inherited by the discrete formulation for arbitrary time step size. Indeed, from Eq. (22) one gets

$$\begin{cases} \displaystyle\int_\Omega \mu_{n+1/2}^h \frac{\{\{\phi_n^h\}\}}{\Delta t} d\Omega + \int_\Omega \vec{\nabla}\mu_{n+1/2}^h \cdot \vec{\nabla} u_{n+1/2}^h d\Omega = 0, \\ \displaystyle -\int_\Omega \tau \vec{\nabla} u_{n+1/2}^h \cdot \frac{\{\{\vec{\nabla} u_n^h\}\}}{\Delta t} d\Omega + \int_\Omega \vec{\nabla} u_{n+1/2}^h \cdot \vec{\nabla}\mu_{n+1/2}^h d\Omega - \int_\Omega \vec{\nabla} u_{n+1/2}^h \cdot \vec{\nabla} u_{n+1/2}^h d\Omega = 0, \\ \displaystyle \int_\Omega \frac{\{\{\phi_n^h\}\}}{\Delta t}\mu_{n+1/2}^h d\Omega - \int_\Omega \frac{\{\{\phi_n^h\}\}}{\Delta t}\frac{1}{2}\left[f(\phi_{n+1}^h) + f(\phi_n^h)\right] d\Omega + \int_\Omega \frac{\{\{\phi_n^h\}\}^3}{12\Delta t}\left[f_+''(\phi_n^h) + f_-''(\phi_{n+1}^h)\right] d\Omega \\ \displaystyle + \int_\Omega 2\vec{\nabla}\left(\frac{\{\{\phi_n^h\}\}}{\Delta t}\right) \cdot \vec{\nabla}\phi_{n+1/2}^h d\Omega + \int_\Omega \vec{\nabla}\left(\frac{\{\{\phi_n^h\}\}}{\Delta t}\right) \cdot \vec{\nabla}\phi_{n+1/2}^h d\Omega = 0, \\ \displaystyle \int_\Omega \theta_{n+1/2}^h \frac{\{\{\theta_n^h\}\}}{\Delta t} d\Omega + \int_\Omega \vec{\nabla}\theta_{n+1/2}^h \cdot \vec{\nabla}\left(\frac{\{\{\phi_n^h\}\}}{\Delta t}\right) d\Omega = 0. \end{cases} \tag{31}$$

Rearranging Eqs. (31) and using the identities (27) and (29), it follows that

$$\frac{1}{\Delta t}\{\{\mathcal{F}\}\} = -\int_\Omega \vec{\nabla} u_{n+1/2}^h \cdot \vec{\nabla} u_{n+1/2}^h d\Omega - \int_\Omega \frac{\{\{\phi_n^h\}\}^4}{24\Delta t}\left[f_+'''(\phi_{n+\xi_+}^h) - f_-'''(\phi_{n+\xi_-}^h)\right] d\Omega. \tag{32}$$

Since f_+''' is a positive function and f_-''' is negative, the stability condition (19) is proven.

In Eq. (32), the first term corresponds to the physical dissipation, while the second term corresponds to numerical dissipation. The second term tends to zero as we reduce the time step.

Thus, our algorithm, which follows directly from the system of equations (22), is second-order time accurate. This is a consequence of the linear terms being approximated with a midpoint-type method and the nonlinear terms being handled with a higher-order generalization of the trapezoidal rule.

V. NUMERICAL APPROXIMATION AND SOLUTION

Before choosing the finite-element spaces, a few remarks about the nonlinearity of the equations are in order. To reduce the nonlinearity of the system (22) it is useful to linearize the cubic and quadratic terms (ϕ_{n+1}^3 and ϕ_{n+1}^2) in the function $f(\phi)$ in the following form:

$$\left(\phi_{n+1}^h\right)^3 \approx 3\left(\phi_n^h\right)^2\phi_{n+1}^h - 2\left(\phi_n^h\right)^3, \tag{33}$$

$$\left(\phi_{n+1}^h\right)^2 \approx 2\phi_n^h\phi_{n+1}^h - \left(\phi_n^h\right)^2. \tag{34}$$

Linearizing quadratic terms (34) further reduces the order of terms in equations and decrease their nonlinearity (similarly to the previous analyses [23] where the cubic contributions of the kind of $(\phi_{n+1}^h)^3$ were linearized). We note that by linearizing the cubic term, the unconditional stability of the algorithm is lost on a theoretical level. We performed a number of simulations with the linearized algorithm and always found nonincreasing energy in the numerical solutions. Thus, we believe our linearly implicit scheme is a good compromise between stability and efficiency.

After the above remarks on linearization, an approximation for the functions ϕ^h, u^h, μ^h, and θ^h should be done by choosing the finite-element spaces in Eqs. (22). We search the solution using triangular Lagrange elements with quadratic shape functions. Every function can be approximated as a sum of basic functions multiplied by solutions in grid nodes [24]:

$$\begin{aligned} \phi^h_{n+1} &= \sum_i \Phi^i_{n+1}\eta^i_{n+1}, \quad u^h_{n+1} = \sum_i U^i_{n+1}\eta^i_{n+1}, \\ \mu^h_{n+1} &= \sum_i \Psi^i_{n+1}\eta^i_{n+1}, \quad \theta^h_{n+1} = \sum_i \Theta^i_{n+1}\eta^i_{n+1}, \end{aligned} \tag{35}$$

where η^i_{n+1} are the shape functions used for the discretization of the $n+1$ time step, and Φ^i_{n+1}, U^i_{n+1}, Ψ^i_{n+1}, Θ^i_{n+1} are the unknown nodal values of the solution for the functions ϕ^h_{n+1}, u^h_{n+1}, μ^h_{n+1}, and θ^h_{n+1}, respectively. Choosing the same mesh on each time step, we have equal shape functions $\eta^i_{n+1} = \eta^i_n = \eta^i$. In the case of adaptive mesh, the shape functions are not equal, so one would compute integrals containing the shape functions defined on two meshes as it is shown below. Thus, substituting approximations (35) into Eqs. (22) gives

$$\begin{pmatrix} M_{n+1} & \frac{\Delta t}{2}A_{n+1} & 0 & 0 \\ 0 & \frac{2\tau+\Delta t}{\Delta t}A_{n+1} & -A_{n+1} & 0 \\ -P_{n+1}+2A_{n+1} & 0 & M_{n+1} & A_{n+1} \\ A_{n+1} & 0 & 0 & M_{n+1} \end{pmatrix} \begin{pmatrix} \Phi_{n+1} \\ U_{n+1} \\ \Psi_{n+1} \\ \Theta_{n+1} \end{pmatrix} = \begin{pmatrix} M_{n+1,n}\Phi_n - \frac{\Delta t}{2}A_{n+1,n}U_n \\ \frac{2\tau-\Delta t}{\Delta t}A_{n+1,n}U_n + A_{n+1,n}\Psi_n \\ -M_{n+1,n}\Psi_n + P^e - 2A_{n+1,n}\Phi_n - A_{n+1,n}\Theta_n \\ A_{n+1,n}\Phi^n + M_{n+1,n}\Theta^n \end{pmatrix}, \tag{36}$$

where

$$\begin{aligned} M_{n+1} &= \left(\eta^i_{n+1},\eta^j_{n+1}\right), \quad A_{n+1} = \left(\vec{\nabla}\eta^i_{n+1},\vec{\nabla}\eta^j_{n+1}\right), \\ P_{n+1} &= \left(\left\{2\alpha\phi_n + 3\phi_n^2 + [1-\varepsilon]\right\}\eta^i_{n+1},\eta^j_{n+1}\right), \\ M_{n+1,n} &= \left(\eta^i_{n+1},\eta^j_n\right), \quad A_{n+1,n} = \left(\vec{\nabla}\eta^i_{n+1},\vec{\nabla}\eta^j_n\right), \\ P^e &= \left(\left\{[1-\varepsilon]\phi_n - \phi_n^3\right\},\eta^i_{n+1}\right), \end{aligned} \tag{37}$$

and $(\cdot,\cdot)$ is the usual scalar product. As a result, Eqs. (36) together with Eqs. (35) and (37) represent Eqs. (22) in the operator form.

VI. BENCHMARKS

In this work only the results of modeling for transformation from unstable state are presented with $\alpha = 0$ in Eqs. (4) and (37). Since the system of equations Eqs. (36) is nonsymmetric it was solved by a generalized minimal residual method (GMRES) solver in the finite-element toolbox FREEFEM++ [25]. We use adapted mesh to the Hessian with the method and algorithm for the mesh generation from Ref. [26].

A. Phase diagram

The computational scheme was used to examine the evolution from a random nonequilibrium state to verify that the scheme does lead to the expected states. This evolution is made in comparison with the phase diagram in the coordinates "undercooling ε–averaged atomic density field $\langle\phi\rangle$" (see, for details, Ref. [2]). In two spatial dimensions, for small values of ε, the phase diagram contains three equilibrium states, a constant homogeneous state, stripes, and a triangular distribution of drops. The regions of phase coexistence are determined by the Maxwell equal-area construction rule [2]: coexisting phases must have equal chemical potentials under constant pressures of the coexisting phases. Sets of equations for two spatial dimensions with "homogeneous state–triangles" and "stripes–triangles" are described as

$$\begin{cases} \mu(\phi_t) = \mu(\phi_h), \\ F_t - F_h = \mu(\phi_h)(\phi_t - \phi_h), \end{cases} \tag{38}$$

$$\begin{cases} \mu(\phi_t) = \mu(\phi_s), \\ F_t - F_s = \mu(\phi_s)(\phi_t - \phi_s), \end{cases} \tag{39}$$

where F, ϕ, and μ are the free energy density, coexistence density of phases, and chemical potentials, respectively. Subscripts t, s, and h denote the corresponding phases: triangles, stripes, and homogeneous, respectively. For small ε these phases can be described by

$$\begin{aligned} \phi_h &= \langle\phi\rangle, \quad \phi_s = A_s\sin(q_s x) + \langle\phi\rangle, \\ \phi_t &= A_t\cos(q_t x)\cos(q_t y/\sqrt{3}) \\ &\quad - A_t\cos(2q_t y/\sqrt{3})/2 + \langle\phi\rangle, \end{aligned} \tag{40}$$

where the quantities q and A give the minimum of the free energy as

$$\begin{aligned} &q_s = 1, \quad A_s = 2\sqrt{\varepsilon/3 - \langle\phi\rangle^2}, \quad q_t = \sqrt{3}/2, \\ &A_t = \tfrac{4}{5}\left(\langle\phi\rangle + \tfrac{1}{3}\sqrt{15\varepsilon - 36\langle\phi\rangle^2}\right). \end{aligned} \tag{41}$$

Free energy densities of phases in the one-mode approximation are given by [2]

$$\begin{aligned} F_h &= (1-\varepsilon)\frac{\langle\phi\rangle^2}{2} + \frac{\langle\phi\rangle^4}{4}, \\ F_s &= -\frac{\varepsilon^2}{6} + \frac{(1+\varepsilon)\langle\phi\rangle^2}{2} - 5\frac{\langle\phi\rangle^4}{4}, \end{aligned} \tag{42}$$

$$\begin{aligned} F_t &= -0.1\left(\varepsilon^2 + \frac{13}{50}\langle\phi\rangle^4\right) + \frac{\langle\phi\rangle^2}{2} \\ &\quad + \frac{4\phi}{25}\sqrt{15\varepsilon - 36\langle\phi\rangle^2}\left(\frac{4}{5}\langle\phi\rangle^2 - \frac{\varepsilon}{3}\right). \end{aligned} \tag{43}$$

Figure 1 shows the regions of the phase existence and coexistence which are divided by the boundaries obtained from the solution of Eqs. (38) to (43). Numerical simulations were conducted at various values of $\langle\phi\rangle$ and ϵ with an initial

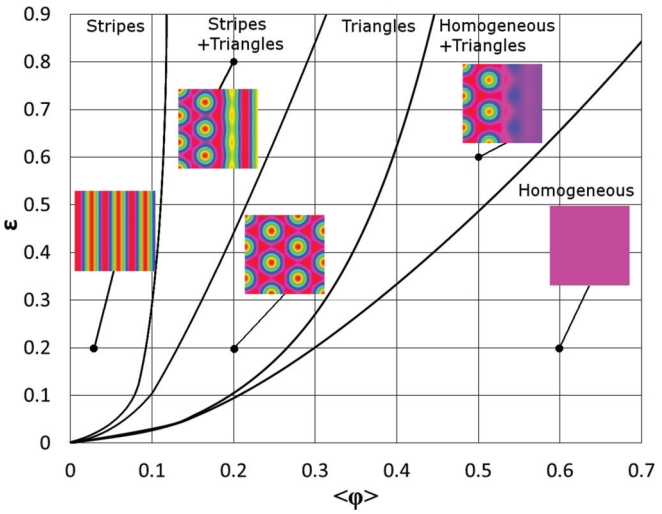

FIG. 1. (Color online) Phase diagram of two-dimensional patterns as predicted by the solution of Eqs. (38) to (43). Solid points indicate initial values for the undercooled homogeneous phase $\langle\phi\rangle$. Pictures in different regions of phase diagram show the finally evolved patterns modeled by Eqs. (36).

condition containing small random fluctuations in ϕ about $\langle\phi\rangle$. The results of the simulated patterns are shown in Fig. 1 and in each case are consistent with analytic one-mode calculations.

Sample time evolutions of the system from a homogeneous to a triangular state are shown in Fig. 2 and from a stripe state to a stripe-triangular coexistence is depicted in Fig. 3. The following parameters where used in these simulations: $(\tau, \langle\phi\rangle, \Delta t, \Delta x) = (0.1, 0.2, 0.01, 0.1)$ in a system of size 190×190 grid points. The undercooling ε was 0.2 and 0.8 for

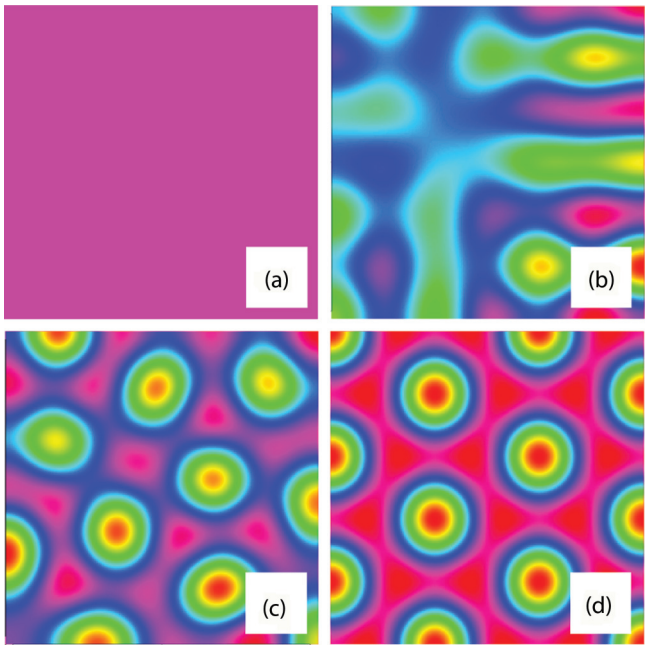

FIG. 2. (Color online) Evolution of the undercooled homogeneous state to stable equilibrium triangle pattern: (a) $t = 0$; (b) $t = 5 \times 10^4$; (c) $t = 10^5$; (d) $t = 2 \times 10^5$. Averaged field $\langle\phi\rangle = 0.2$ has been initially undercooled by $\epsilon = 0.2$.

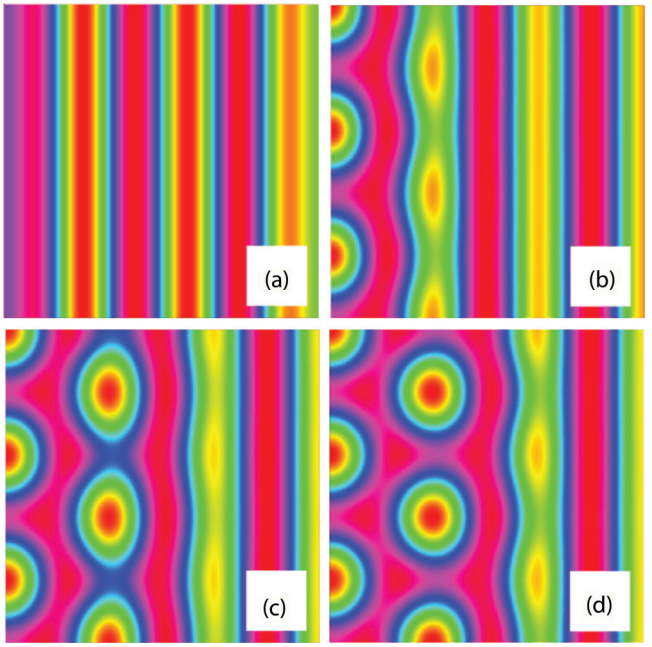

FIG. 3. (Color online) Transformation of undercooled stripes to equilibrium coexistence of stripes and triangles: (a) $t = 0$; (b) $t = 5 \times 10^4$; (c) $t = 10^5$; (d) $t = 2 \times 10^5$. Averaged field $\langle\phi\rangle = 0.2$ has been initially undercooled by $\epsilon = 0.8$.

Figs. 2 and 3, respectively. Both results are consistent with the calculated phase diagram shown in Fig. 1.

We also note that the boundaries in the phase diagram of Fig. 1 have been calculated using one-mode approximation which is the first approximation to solution of the PFC equation (9) only at small undercooling ε and $\tau \to 0$. Consequently the numerical solutions will deviate from the analytic calculations for larger undercoolings.

B. Unconditional stability

The algorithm and discrete scheme deliver unconditional stability of numerical computations. The time step Δt can be arbitrary chosen and it is limited only by the requirement of computational accuracy. The stability of the presented algorithm has been verified numerically in a series of computations with different values for space and time discretization.

To demonstrate unconditional stability, the evolution of the free energy is analyzed. The free energy (1) to (4) has been taken in the following form:

$$\mathcal{F}(\phi, \vec{J}) = \int_\Omega \left[F(\phi) - |\vec{\nabla}\phi|^2 + \frac{1}{2}(\nabla^2\phi)^2 + \frac{\tau}{2}|\vec{\nabla}u|^2 \right] d\Omega. \tag{44}$$

The energy (44) is defined by a local equilibrium part described by the slow variable ϕ and a local nonequilibrium part, $\propto J^2 = |\vec{\nabla}u|^2$, corresponding to the kinetic contribution of the free energy [27] in terms of the fast variable $\vec{J}$. Thus, we shall plot the evolution of the energy (1) to (4).

Figure 4 shows the evolution of the free energy functional $\mathcal{F}$ described by Eq. (44) for different values of the relaxation time τ. As it can be seen, $\mathcal{F}$ monotonically decreases during the computational time $0 < t < t^*$ for the transition from the

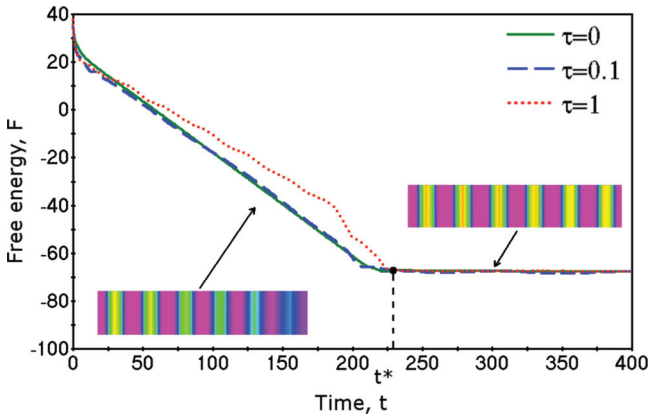

FIG. 4. (Color online) Transition from initially homogeneous state to stripes. The homogeneous state has been quenched at $\varepsilon = 0.2$ and $\langle\phi\rangle = 0.02$. Numeric parameters were chosen as $(\Delta t, \Delta x) = (0.005, 0.1)$. The free energy functional $\mathcal{F}$ from Eq. (44) decreases monotonically with time for the developing stripes during the computational time $0 < t < t^*$ (see the developing pattern in the left part). The free energy functional $\mathcal{F}$ has a constant values in modeling with $t > t^*$ (see the steady pattern in the right part).

initially undercooled homogeneous state to stripes. With $t > t^*$, the steadily stable stripes exhibit a constant value of $\mathcal{F}$ for all values of τ tested in this work. The behavior of $\mathcal{F}$ shown in Fig. 4 is similar to that obtained for the crystal growth in a supercooled liquid described by the parabolic PFC equation (see Fig. 2 in Ref. [20]). This clearly supports our theoretical results obtained for the algorithm, computational scheme, and approximation of functions.

VII. VELOCITY AND WAVE NUMBER AT THE FRONT INVADING UNSTABLE PHASE

Patterns that emerge when the interface or front invades an excitable or unstable media have been of interest in many physical phenomena [28]. In this section the numerical method developed in this work will be used to find the velocity and wavelength of a periodic pattern that emerges as a phase front sweeps through an unstable phase. The results can be quantitatively compared with the predictions of the marginal stability analysis on the wavelength selection at the front of periodic pattern described by the hyperbolic PFC equation [22]. The predictions for front velocities and wavelength selection from marginal stability have been numerically verified in other pattern forming models, such as a phase field model of a superheated solid invading an undercooled melt at large undercoolings [29].

A. Marginal stability analysis

Let us consider a front between a periodic striped pattern and a spatially homogeneous unstable state at $\langle\phi\rangle \to 0$, such the periodic state is the lowest energy state for all undercoolings, ε (see the phase diagram plotted in Fig. 1). The situation is depicted in Fig. 5. The goal of this work is to determine the velocity (V) of the front and the periodicity of the pattern selected near the front (which is different from the equilibrium wavelength). Far enough in ahead of the front the

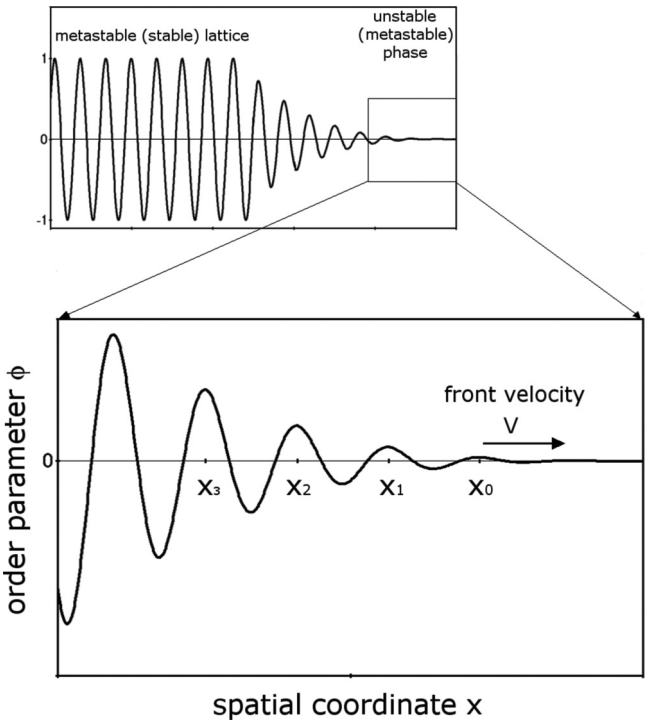

FIG. 5. Front of periodic pattern described by PFC model. The selected lattice parameter (or wavelength) on the front invading un(meta)stable phase should be measured at the farthest away point significant growth of amplitude of periodic pattern as is shown in the inset. x_0 is the point from which the lattice parameter (wavelength) begins to be calculated.

equation of motion can be linearized around the homogeneous state (i.e., $\phi = \delta\phi + \langle\phi\rangle$) in a moving reference frame and solutions for velocity and periodicity can be obtained using the marginal stability condition as described by the authors of Ref. [22]. Briefly this calculation first determines the linear dispersion rate at the front, which is given by

$$\omega(k) = \frac{1}{2\tau}[\sqrt{1 + 4\tau\xi(k)} - 1] + iVk, \quad \text{with} \quad \xi(k) = k^2[\epsilon - (1 - k^2)^2], \tag{45}$$

where $\delta\hat{\phi} \propto \exp[\omega(k)t]$, k is the wave number and $\delta\hat{\phi}$ is the Fourier transform of $\delta\phi$. A perturbation is marginally stable at the moving front for $\mathrm{Re}[\omega(k)] = 0$, i.e., the front neither grows nor decays exponentially at the amplification rate (45) as

$$V = \frac{1}{k^*_{\mathrm{im}}}\mathrm{Re}\left\{\frac{1}{2\tau}[\sqrt{1 + 4\tau\xi(k^*)} - 1]\right\}. \tag{46}$$

Here k^* is the selected wave number assumed to be complex valued, $k^* = k^*_{\mathrm{re}} + ik^*_{\mathrm{im}}$ where k^*_{re} and k^*_{im} are the real and imaginary parts, respectively.

The most unstable mode at the front of the periodic stripes is given by the saddle point $\partial\omega/\partial k = 0$ with $k = k^*$. Using the amplification rate (45), the saddle-point condition gives

$$iV + \frac{2k^*[\epsilon - 1 + 4(k^*)^2 - 3(k^*)^4]}{\sqrt{1 + 4\tau\xi(k^*)}} = 0. \tag{47}$$

Finally, the selection of the wave number k_f at the front oscillating at angular frequency $\mathrm{Im}[\omega(k^*)]$ is defined by

$$k_f = \frac{\mathrm{Im}[\omega(k^*)]}{V}. \tag{48}$$

Using Eq. (45), the system of equations (46) to (48) was solved numerically [22] to predict the selection of the wave number $k_f(\varepsilon)$ and lattice parameter $a_f(\varepsilon) = 2\pi/k_f(\varepsilon)$ at the front moving with the velocity $V(\varepsilon)$.

B. Algorithm for numerical results of the velocity and wave number

The velocity and wave number selected can be obtained by direct numerical simulation of the PFC equation. After reaching a stationary regime the determination of these quantities was obtained using the following algorithm.

(1) Find the peak or maximum with a height above $\phi \geqslant \langle\phi\rangle + 0.1$ farthest from the initial perturbation position. This peak will be denoted x_0, the next farthest as x_1, and so on, as shown in Fig. 5. The distance between successive peaks can then be used to calculate the selected lattice parameter or wave vector.

(2) Compute the distances between neighboring peaks (see the inset in Fig. 5). Then, the required lattice parameters a_i are

$$a_0 = x_0 - x_1, \quad a_1 = x_1 - x_2, \quad a_2 = x_2 - x_3,$$
$$a_{01} = \frac{a_0 + a_1}{2}, \quad a_{12} = \frac{a_1 + a_2}{2}. \tag{49}$$

Calculate the average lattice parameter by its mean value

$$a = \frac{a_{01} + a_{12}}{2}. \tag{50}$$

(3) After the calculation of the lattice parameter a, the wave number k_f on the front is computed by $k_f = 2\pi/a$.

(4) Calculate the front velocity as a displacement of the initial point x_0 divided by the time step: $V = [x_0(t + \Delta t) - x_0(t)]/\Delta t$.

Calculated values of the wave number k_f are strongly dependent on the computational grid used in numerical simulations. With the refinement grid, the values of k_f converge to the value necessary to obtain the prediction. As an example, Table I gives values for wave numbers $k(a_i)$ calculated with different grids and from the values of the lattice parameter a_i given by Eqs. (49) and (50).

TABLE I. Modeling predictions for wave numbers calculated for different grids and various averaged procedures.

ε	mesh	$k(a_0)$	$k(a_1)$	$k(a_2)$	$k(a_{01})$	$k(a_{12})$	$k(a_{02})$	$k(a)$
0.1	regular	1.047	1.026	1.026	1.036	1.026	1.036	1.033
	adapted	1.023	1.016	1.010	1.020	1.013	1.016	1.016
0.4	regular	1.169	1.169	1.1424	1.169	1.1555	1.1555	1.16
	adapted	1.1284	1.1152	1.1010	1.1218	1.1080	1.1145	1.1148
0.6	regular	1.226	1.197	1.197	1.211	1.197	1.211	1.206
	adapted	1.195	1.180	1.161	1.187	1.170	1.178	1.178

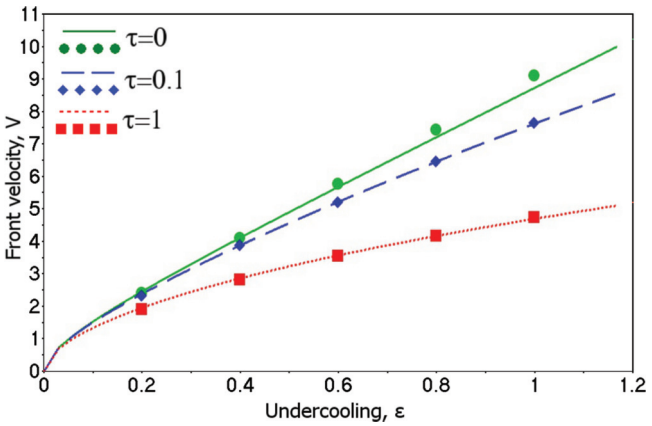

FIG. 6. (Color online) Velocity V of the PFC front versus undercooling ε as given by the results of present modeling (points) in comparison with the marginal stability predictions (curves), Eqs. (45) to (48).

C. Comparison

For the numerical calculations the initial condition was such that $\phi_{x>0} = 0$ and $\phi_{x=0}$ have been set to be random numbers chosen between 0 and 0.01. The initial size of the system was 1000×10, with a grid spacing of the initial regular mesh $h = 0.125$ and a minimal grid spacing in the adapted mesh as $h_{\min} = 1 \times 10^{-4}$. This grid was used to obtain the results summarized in Table I. The size of this system is large enough that steady state profiles were obtained before the boundary conditions interfered.

Our computational domain has been chosen to be a quasi-one-dimensional region to provide comparison to the marginal stability analysis [22] in one-dimensional space. All comparisons for the wavelength selection have been made for the stripes. In the numerical simulations the stripes propagate in the direction perpendicular to their geometrical axes.

The marginal stability results are only valid far from the front in which the linearization is valid. For this reason the comparison should work the best farthest from the front. The inset in Fig. 5 gives an example of the peak positions chosen for the study. A comparison of the numerically calculated front velocity and wave number (dots in plots) with the predictions of the marginal stability described by Eqs. (45) to (48) (lines in plots) are summarized in Figs. 6 and 7, respectively. It can be seen from Fig. 6 that the velocity V obtained in the present modeling for the stripes' propagation is perfectly consistent with the front velocity described by the criterion of marginal stability. The wave number k calculated on the front of the modeled stripes is also consistent with k_f selected on the front of the periodic pattern analytically predicted by the marginal stability criterion (Fig. 7). Although the calculated wave numbers (see circles, diamonds, and squares in Fig. 7) exhibit some deviations from the curves given by the marginal stability criterion, they depend on their averaged values obtained for different computational grids (see Table I) and from the wavelengths for different peaks in a periodic pattern on the front (see the inset in Fig. 5). As a result, the wave numbers obtained in the present modeling have error bars which include the curves given by the criterion of marginal stability (see Fig. 7). Hence, the present numerical algorithm

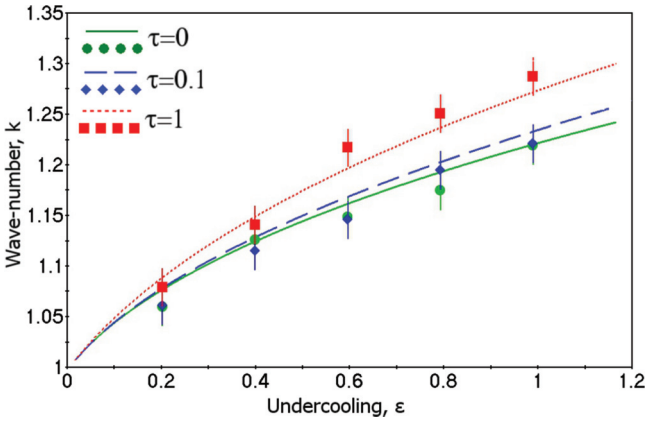

FIG. 7. (Color online) Wave number k_f selected at the PFC front as a function of undercooling ε. The present modeling results (points) are compared to the predictions of marginal stability analysis (curves), Eqs. (45) to (48).

and its numerical realization exhibit quantitative agreement with the results obtained from the marginal stability analysis described by Eqs. (45) to (48).

VIII. CONCLUSION

An unconditionally stable time integration algorithm for the solution of the hyperbolic PFC model equation is presented. Variational formulation of the model has allowed us to use a finite-element method for numerical simulation using standard C^0-continuous Lagrange elements (available in modern program packages). As a result, a second-order accurate finite-element numerical scheme has been developed, which is unconditionally stable and ensures that free energy decreases as patterns evolve and become constant in the steady state.

The numerical scheme was shown to give results consistent with the phase diagram of the model constructed from a one-mode approximation in the appropriate limit. Additionally the scheme was shown to be quantitatively consistent with the predictions of marginal stability theory for velocity and wave-vector selection of a striped phase invading an unstable homogeneous state. These results confirm the applicability of the present algorithm and numerical scheme to theoretically important and practically significant quantitative predictions.

ACKNOWLEDGMENTS

P.K.G. acknowledges the partial support within the framework of the program 07.08 "Research Investigations in Education" Project No. 2.947.2011. P.K.G. is also grateful for support from the Faculty of Physics during his stay in Oakland University (Rochester, MI). H.G. acknowledges support from Xunta de Galicia and the European Research Council through the FP7 Ideas Starting Grant program (Project No. 307201). N.V.K. thanks support from German Foundation of Scientific Exchanges, Stipendium A/11/94255 (DAAD: Deutscher Akademischer Austausch Dienst). K.R.E. acknowledges support from NSF under Grant No. DMR-0906676.

[1] K. R. Elder, M. Katakowski, M. Haataja, and M. Grant, Phys. Rev. Lett. **88**, 245701 (2002).
[2] K. R. Elder and M. Grant, Phys. Rev. E **70**, 051605 (2004).
[3] K. R. Elder, G. Rossi, P. Kanerva, F. Sanches, S.-C. Ying, E. Granato, C. V. Achim, and T. Ala-Nissila, Phys. Rev. Lett. **108**, 226102 (2012).
[4] K. R. Elder, N. Provatas, J. Berry, P. Stefanovic, and M. Grant, Phys. Rev. B **75**, 064107 (2007).
[5] T. V. Ramakrishnan and M. Yussouff, Phys. Rev. B **19**, 2775 (1979); R. Evans, Adv. Phys. **28**, 143 (1979); Y. Singh, Phys. Rep. **207**, 351 (1991).
[6] Y. M. Jin and A. G. Khachaturyan, J. Appl. Phys. **100**, 013519 (2006).
[7] H. Emmerich, H. Löwen, R. Wittkowski, T. Gruhn, G. I. Tóth, G. Tegze, and L. Gránásy, Adv. Phys. **61**, 665 (2012).
[8] P. Stefanovic, M. Haataja, and N. Provatas, Phys. Rev. Lett. **96**, 225504 (2006); Phys. Rev. E **80**, 046107 (2009).
[9] P. Galenko, D. Danilov, and V. Lebedev, Phys. Rev. E **79**, 051110 (2009).
[10] J. A. P. Ramos, E. Granato, S. C. Ying, C. V. Achim, K. R. Elder, and T. Ala-Nissila, Phys. Rev. E **81**, 011121 (2010).
[11] S. M. Wise, C. Wang, and J. S. Lowengrub, SIAM J. Numer. Anal. **47**, 2269 (2008).
[12] V. Lebedev, A. Sysoeva, and P. Galenko, Phys. Rev. E **83**, 026705 (2011).
[13] C. Wang and S. M. Wise, SIAM J. Numer. Anal. **49**, 945 (2011).
[14] A. Baskaran, J. S. Lowengrub, C. Wang, and S. M. Wise, SIAM J. Numer. Anal. (to be published).
[15] D. J. Eyre, An unconditionally stable one-step scheme for gradient systems (unpublished), www.math.utah.edu/~eyre/research/methods/stable.ps.
[16] D. J. Eyre, in *Computational and Mathematical Models of Microstructural Evolution*, MRS Proceedings Vol. 529, edited by J. W. Bullard, L. Q. Chen, R. K. Kalia, and A. M. Stoneham (The Materials Research Society, Warrendale, PA, 1998), p. 39–46.
[17] B. P. Vollmayr-Lee and A. D. Rutenberg, Phys. Rev. E **68**, 066703 (2003).
[18] M. Cheng and J. A. Warren, Phys. Rev. E **75**, 017702 (2007); J. Comp. Phys. **227**, 6241 (2008).
[19] H. Gomez and T. J. R. Hughes, J. Comp. Phys. **230**, 5310 (2011).
[20] H. Gomez and X. Nogueira, Comput. Methods Appl. Mech. Engrg. **249**, 52 (2012).
[21] H. Gomez, V. M. Calo, Y. Bazilevs, and T. J. R. Hughes, Comput. Methods Appl. Mech. Engrg. **197**, 4333 (2008).
[22] P. K. Galenko and K. R. Elder, Phys. Rev. B **83**, 064113 (2011).
[23] R. Backofen, A. Rätz, and A. Voigt, Philos. Mag. Lett. **87**, 813 (2007).
[24] O. K. Zienkiewicz, *The Method of Finite Elements in Engineering* (McGraw-Hill, New York, 1977); L. J. Segerlind, *Applied Finite Element Analysis*, 2nd ed. (Wiley, New York, 1984).

[25] http://www.freefem.org.

[26] F. Hecht, The mesh adapting software: bamg. INRIA report 1998, http://www-rocq.inria.fr/gamma/cdrom/www/bamg/eng.htm; B. Mohammadi and F. Hecht, Revue Européene des Éléments Finis **10**, 575 (2001).

[27] P. Galenko and D. Jou, Phys. Rev. E **71**, 046125 (2005); Physica A **388**, 3113 (2009).

[28] G. Dee and J. S. Langer, Phys. Rev. Lett. **50**, 383 (1983); E. Ben-Jacob, H. Brand, G. Dee, L. Kramer, and J. S. Langer, Physica D **14**, 348 (1985); W. van Saarlos, Phys. Rep. **386**, 29 (2003); R. Goh, S. Mesuro, and A. Scheel, SIAM J. Appl. Dyn. Sys. **10**, 360 (2011).

[29] M. Zukerman, R. Kupferman, O. Shochet, and E. Ben-Jacob, Physica D **90**, 293 (1996).